NUCL SCI TECH (2021) 32:135
https://doi.org/10.1007/s41365-021-00978-9

Fabrication of stable MWCNT bucky paper for solar-driven interfacial evaporation by coupling γ-ray irradiation with borate crosslinking

Yu-Qing Qiao[1] · Yu Gu[2,3] · Yu-Sen Meng[1] · Hai-Xia Li[3,4] · Bo-Wu Zhang[1] · Jing-Ye Li[1,3]

Received: 25 August 2021 / Revised: 1 November 2021 / Accepted: 7 November 2021 / Published online: 8 December 2021

Abstract Herein, we report a facile solution process for preparing multi-walled carbon nanotube (MWCNT) bucky paper for solar-driven interfacial water evaporation. This process involves vacuum filtrating a dispersion of MWCNTs that was modified by polyvinyl alcohol (PVA) under γ-ray irradiation on a cellulose acetate microporous membrane, followed by borate crosslinking. Fourier transform infrared spectroscopy, Raman spectroscopy, and thermogravimetry confirmed the success of PVA grafting onto MWCNTs and borate crosslinking between modified MWCNT nanoyarns. The as-prepared crosslinked MWCNT bucky papers (BBP membranes) were used as a solar absorber, by placing them on a paper-wrapped floating platform, for interfacial water evaporation under simulated solar irradiation. The BBP membranes showed good water tolerance and mechanical stability, with an evaporation rate of 0.79 kg m^{-2} h^{-1} and an evaporation efficiency of 56% under 1 sun illumination in deionized water. Additionally, the BBP membranes achieved an evaporation rate of 0.76 kg m^{-2} h^{-1} in both NaCl solution (3.5 wt%) and sulfuric acid solution (1 mol L^{-1}), demonstrating their impressive applicability for water reclamation from brine and acidic conditions. An evaporation rate of 0.70 kg m^{-2} h^{-1} (very close to that from deionized water) was obtained from the solar evaporation of saturated NaCl solution, and the BBP membrane exhibited unexpected stability without the inference of salt accumulation on the membrane surface during long-term continuous solar evaporation.

Keywords γ-ray irradiation · Multi-walled carbon nanotubes · Bucky paper · Solar-driven interfacial water evaporation · Desalination

1 Introduction

The shortage of drinking water has become an increasing global crisis and challenge, along with population growth, industrialization, and environmental pollution. To address this issue, many technologies have been developed to effectively desalinate seawater or decontaminate wastewater, including reverse osmosis, distillation, evaporation, and electrodialysis [1]. Solar-driven interfacial water evaporation is an emerging technology that has attracted great attention owing to its high efficiency, sustainability, and low cost [2]. It simultaneously localizes solar energy harvesting and steam generation at the water–

This work was financially supported by the National Natural Science Foundation of China (Grants 11875313 and 12075153).

Yu-Qing Qiao and Yu Gu contributed to this work equally.

✉ Bo-Wu Zhang
zhangbowu@shnu.edu.cn

✉ Jing-Ye Li
jyli@shnu.edu.cn

[1] MOE Key Lab of Resource Chemistry, Shanghai Key Lab of Rare Earth Functional Materials, College of Chemistry and Materials Science, Shanghai Normal University, Shanghai 200234, China

[2] Yellow River Institute of Eco-Environmental Research, Yellow River Basin Ecology and Environment Administration, Zhengzhou 450000, China

[3] Shanghai Institute of Applied Physics, Chinese Academy of Sciences, Shanghai 201800, China

[4] School of Civil and Architectural Engineering, Nanjing Tech University Pujiang Institute, Nanjing 211134, China

air interface. However, its large-scale application is still limited by the complex fabrication, leaching, and disposal of synthetic photothermal conversion materials [3]. Several kinds of synthetic photothermal conversion materials have been utilized for solar-driven interfacial water evaporation [4]. The first is plasmonic nanostructures, mainly including Au, Ag, Pd, Cu, Ni, and other metallic nanoparticles [5, 6], where the light-driven surface plasmon resonance (SPR) effect (also called surface plasmon polarization) is the mechanism of light-to-heat conversion [4]. When the frequency of incident light matches the resonance frequency of the delocalized electrons on the surface of a metal, collective excitation of electrons occurs and generates hot electrons. The hot electrons coherently oscillate with the incident electromagnetic field, resulting in heat energy by the Joule mechanism [7, 8]. However, plasmonic nanomaterials for solar-to-heat conversion still suffer many challenges, such as a narrow absorption spectrum bandwidth and high dependence on the sharpness and size of nanostructures [8], which particularly affects the material cost for large-scale applications [5].

Low-cost and low-toxicity inorganic semiconductors have emerged as photothermal conversion materials for solar evaporation, such as defect-rich metal oxide semiconductors and intrinsic semiconductors with narrow band gaps. Defect-rich semiconductors, such as reduced tungsten oxide, iron oxides, molybdenum oxides, and titanium dioxides, strongly absorb light with an energy similar to their bandgap and convert it into heat through the nonradiative recombination of electron–hole pairs [6]. Conversely, intrinsic semiconductors can absorb photons with energies higher than their band gaps, where the electrons excite from the valence band to the conduction band and return to the edge of the conduction band releasing heat energy due to a relaxation effect [9]. Although many efforts have been made to broaden the absorption spectra of semiconductor materials [10], they are still much narrower than the emission spectrum of sunlight. Conjugated polymers, such as polyaniline and polypyrrole, have also attracted much interest in solar heat applications owing to their unique optical activity, low cost, light weight, and facile chemical synthesis. Owing to the substantial π-electron delocalization in their structures, conjugated polymers easily absorb light in the visible and near-infrared regions, which cause lattice vibrations by charge transfer that generate heat in the materials. Additionally, melanin-based natural organic materials (e.g., indolic polymers and polydopamine [11]) are also capable of converting light to heat energy owing to their high degree of molecular conjugation. However, these organic photothermal materials also suffer from either a narrow light absorption range, poor photostability, or limited practical applications [9].

Unlike conjugated polymers, all-carbon materials are electrical conductors with zero band gap. Thus, they can strongly absorb light across the entire solar spectrum like a black body, and convert it to heat through lattice vibrations [9]. Carbon nanodots, carbon nanotubes (CNTs), graphene, and its derivatives, graphite, carbon black, porous carbon, and biomass-derived amorphous carbon have been widely used as low-cost, lightweight, scalable, and effective photothermal materials for solar interfacial evaporation [12]. Many two-dimensional and three-dimensional composite photothermal materials based around the carbon system, such as metal–organic framework carbon materials [13] and graphene aerogel [14], have been extensively researched and used in steam-power generation [15], sewage adsorption treatment [16], sterilization, and other fields [17]. Compared with the aforementioned photothermal conversion materials, all-carbon materials have advantages, such as cost efficiency, ready availability, broad absorption spectra, high photothermal conversion efficiency, outstanding chemical stability, and environmental friendliness. These properties demonstrate that all-carbon materials are the most promising photothermal material candidates for large-scale practical applications. Nevertheless, the high stability of carbon-based materials restricts the construction of desirable macroscopic shapes for solar thermal applications with porous structures. As a representative all-carbon material, CNTs are capable of forming vertically aligned carbon nanotube (VACNT) forests, exhibiting extremely low reflectance and broad absorption spectra [9]. These VACNT forests can only be prepared by chemical vapor deposition (CVD), which makes them difficult to use for solar interfacial evaporation on a large scale. CNT-based bucky paper, a paper-like entangled CNT assembly, has a hierarchically interconnected porous architecture. This structure provides more water channels and improves water permeability [18, 19]. This promotes water stream effusion from the water–air interface, thereby enhancing the solar evaporation [20]. CNT-based bucky paper has a random arrangement of CNTs and can be conveniently prepared through conventional solution processes. However, bucky paper is often fragile owing to the weak connections between CNT yarns [21]. In addition, individual CNT yarns broken from the bucky paper are released into the environment, possibly triggering biological consequences of animal overexposure to CNTs [22, 23], such as oxidative stress [24], interference with cell signaling pathways [25], and membrane disruption [26]. Therefore, the connections between CNT yarns should be reinforced to ensure the safety and durability of the bucky paper for practical applications. Intercalating various polymer materials into the bucky paper is a simple and effective way to enhance its mechanical properties [27]. For example, the Young's modulus, tensile strength, toughness, and strain-to-break values of bucky paper can be increased by introducing poly(vinylpyrrolidone) [27, 28], poly(vinyl alcohol) (PVA) [29], poly(norbornene) [30], epoxy resin [31], or biopolymers [32] through coating or immersion. However, in most cases, the polymers in the bucky paper interact with the CNT yarns in a non-covalent manner, which results in the easy loss of polymers by solvent erosion. Therefore, boosting the interactions between polymer chains and CNTs is a major challenge in the construction of a functional bucky paper or other types of CNT-based membranes. Clearly, covalently linking the nanotubes with polymer chains is a feasible way to investigate the loss of polymers and boost the durability of the bucky paper [33, 34]. Unfortunately, CNTs are well-known to be inert to most chemical reactions by conventional methods unless they are treated via sophisticated processes under harsh conditions, which is unfavorable for large-scale production.

Radiation technology is a powerful and scalable technical means for material production and modification. It has been widely used in industrial processes (i.e., heat-shrink tubing, battery membranes, and vulcanizing rubber) and waste degradation [35], and academic research, such as radiation syntheses of inorganic nanoparticles [36], functional polymers [37], and covalent organic frameworks (COF) [38], radiation degradation of organic pollutants [39], and radiation functionalization of polymeric composites [40]. These methods utilize the strong ionizing effects of high-energy radiation, mainly involving γ-rays from Co-60 or Cs-137 sources and electron beams from electron accelerators. This radiation directly or indirectly creates reactive radicals, further initiating various chemical reactions with no catalysis or extreme operating conditions. Owing to this crude but effective process, radiation technology has been utilized to functionalize various nanocarbon materials, such as CNTs [41], nanodiamonds, fullerene [42], carbon nanofibers [43], and graphene and its derivatives [44], through grafting polymerization [41], crosslinking [45] and etching reactions [46]. Recently, our group developed a radiation-induced “grafting to” method for the modification of polyvinylidene fluoride [47], graphene oxide [48], and multi-walled carbon nanotubes (MWCNTs) [49], which was simply implemented by immersing substrates in polyvinyl alcohol (PVA) solution prior to irradiating with γ-rays. This route can easily decorate substrates with polymeric chains on a large scale, endowing nanocarbons with good dispersibility in solution. Based on a previous study, we designed a facile solution process to prepare robust MWCNT bucky paper by combining radiation modification and borate crosslinking of the PVA chains on MWCNTs. Fourier transform infrared (FT-IR) spectroscopy, Raman spectroscopy, and thermogravimetry (TG) were utilized to confirm the success of PVA grafting onto MWCNTs and borate crosslinking. In addition, MWCNT bucky paper was prepared by vacuum filtration of the grafted MWCNT dispersion on cellulose acetate (CA) microporous membranes, and their micromorphology and surface properties were characterized. Additionally, the obtained MWCNT bucky paper was further studied for water reclamation through solar-driven interfacial water evaporation under high salt and acidic conditions, to demonstrate its durability under harsh conditions.

2 Experimental section

2.1 Materials and chemicals

MWCNTs (L-MWNT-4060, 95%, 40–60 nm outer diameter, and 5–15 μm length) were purchased from Shenzhen Nanotech Port Co., Ltd. (Shenzhen, China). PVA (1788) granules, concentrated sulfuric acid (95%–98%), phosphoric acid (AR, ≥ 85%), nitric acid (65%–68%), hydrochloric acid (36%–38%), boric acid, sodium chloride, and ethanol were obtained from Sinopharm Chemical Reagent Co., Ltd. (China). Commercial CA membranes (0.45 μm) were purchased from Shanghai Xingya Purification Material Factory (China). All materials and reagents were used as received without further purification unless mentioned otherwise, and the water used in this study was deionized.

2.2 Fabrication of MWCNTs-g-PVA powder

Pristine MWCNTs were purified by heating under reflux in a mixed HNO_3/H_2SO_4 solution (v/v = 3/1), as reported previously [49] and the product was labeled as oxidized MWCNTs. Thereafter, 0.255 g of oxidized MWCNTs and 25.5 g of PVA solution (10 wt%) were added to an ethanol/water solution (v/v = 1/1) to obtain a mixed solution of 250 g in mass. The mixed solution was sealed without degassing and placed in a cobalt 60 source chamber at room temperature for an absorbed dose of 34 kGy at a dose rate of 2 kGy h^{-1}. After irradiation treatment, the solution was centrifuged at 8000 rpm (SF-TGL-20A, Shanghai Feiqiaer Analytical Instrument Co., Ltd., China) for 15 min, and the resulting supernatant was centrifuged at 10,000 rpm prior to collecting the precipitate. After three repeated purifications by washing and centrifugation, the precipitate was dried at 60 °C in a vacuum drying oven. The resulting MWCNTs-g-PVA powder was analyzed using a TG instrument to determine its degree of grafting (DG) as 17.2% according to a previously reported calculation method [50].

2.3 Preparation of modified MWCNT bucky paper

After repeating the above steps of powder oxidation and radiation modification, the black supernatant was collected by centrifugation of the irradiated mixed solution at 8000 rpm. The supernatant was then vacuum filtered to deposit MWCNTs-g-PVA onto a CA microporous membrane with a diameter of 0.45 μm. After washing with a large volume of hot water, the obtained MWCNT bucky paper was dried at room temperature and named as the BP membrane. Three BP membranes with different thicknesses of functional layers were prepared by controlling the mass of MWCNTs-g-PVA deposited on CA membranes to evaluate the influence of the powder mass on the membrane properties. The three membranes were labeled as BP-1, BP-2, and BP-3, corresponding to MWCNTs-g-PVA powders of 0.55 g m^{-2}, 0.83 g m^{-2}, and 2.31 g m^{-2}, respectively. These three membranes were immersed separately in a boric acid solution (4 wt%) for 12 h to form borate-based linkages between PVA chains from different yarns. After the crosslinking treatment, the membranes were washed with a large amount of deionized water, air-dried, and named as BBP-1, BBP-2, and BBP-3, for the crosslinked equivalents of the BP-1, BP-2, and BP-3 membranes, respectively.

To determine the boric crosslinking extent, the grafted MWCNT powder was dispersed in boric acid (4 wt%) aqueous solution for 12 h at room temperature and then purified by water washing and centrifugation at 10,000 rpm for 10 min for a minimum of three times. After drying in a vacuum oven at 60 °C overnight, a boric-crosslinked MWNTs-g-PVA powder was obtained and subsequently characterized by chemical analyses.

2.4 Solar-driven interfacial water evaporation

The solar water evaporation device used in our study consists of three parts: a simulated solar light source, a water evaporation container, and an analytical balance. The light source was a xenon lamp (CME-SL500, Zhongke Microenergy Tech. Co., Ltd., China). The main body of the water evaporation device was a 500-ml beaker wrapped with black foam to reduce heat loss. A floating platform made of filter paper-covered polystyrene (PS) foam was cut into a shape with Φ = 4 cm × 0.5 cm. Owing to its low density and thermal conductivity ($0.035 - 0.052$ W m^{-1} K^{-1}), the PS foam floated on the water in the beaker as a thermal isolator. A crossed slit was made in the center of the foam into which a filter paper strip was inserted, which acted as the water channel to continuously transport water to the filter paper on the top of the foam. A BP or BBP membrane was placed on the filter paper and evenly wetted by water. The material cost of the entire evaporator was approximately 300 RMB m^{-2}. The evaporation container was placed on an analytical balance during the test to measure the water mass loss over the illumination time. During the test, a thermal infrared imager (Xtherm T2S, Ray Tech. Co., Ltd., China) was used to record the temperature change of the sample surface, and an optical power meter (TES-132, TES Electrical Electronic Corp., China) was used to monitor the radiation intensity of the simulated light source. The ambient temperature during the tests was approximately 20 °C, and the relative humidity was approximately 65%. After a single test, the filter paper was replaced and the solar water evaporation device was allowed to return to the ambient temperature before a new test was started.

The water evaporation rate ($\dot{m}$, kg m^{-2} h^{-1}) and solar evaporation efficiency (η, %) were calculated as follows:

$$\dot{m} = \Delta M/(S \times \Delta t), \tag{1}$$

$$\eta = (\dot{m}(Lv + Q))/(C \times P), \tag{2}$$

$$Q = c\Delta M(T_1 - T_0), \tag{3}$$

where ΔM is the change in water mass; S is the effective evaporation area of the evaporator; Δt is the evaporation duration time; Lv denotes the evaporation enthalpy of the water body (generally 2260 kJ kg^{-1}); Q is the sensible heat of the water (the energy required for temperature rising from the initial to the evaporation); C is the surface optical intensity of the optical absorber; P is the incident light intensity (kJ m^{-2} h^{-1}); c refers to the specific heat of water (4.2 kJ kg^{-1} K^{-1}); T_1 and T_0 are the temperatures of the evaporation surface and the initial water temperature, respectively [4].

2.5 Instruments and characterization

FT-IR spectra of the powders were recorded using the potassium bromide pellet method on a Bruker Optics TENSOR 27 FT-IR spectrometer and scanning in the wavenumber region 4000–650 cm^{-1} at a spectral resolution of 4 cm^{-1}. Raman analyses of the powder samples were performed on a Raman spectrometer (Xplora INV, France) with an excitation wavelength of 633 nm. All samples were dried in a vacuum oven overnight before testing. The micromorphological observation of the bucky papers was performed using a field-emission scanning electron microscope (Merlin compact, Zeiss, Germany) at an operating voltage of 10 kV. The cross section was observed by breaking the samples in liquid nitrogen and sputtering with gold before imaging. TG curves were obtained from a TG 209 F3 Tarsus Thermo Microbalance (NETZSCH Instruments Co., Germany) using an aluminum oxide crucible under nitrogen purging (50 mL min^{-1}) at a heating rate of 10 °C min^{-1}. UV–vis-

NIR absorption spectra were recorded by Shimadzu UV-3600 at 300–2000 nm. Micromorphological observation was performed on a scanning electron microscope (SEM) (S-4800, Hitachi Co., Japan).

3 Results and discussion

Scheme 1 presents the preparation process of the MWCNT bucky paper by γ-ray irradiation and borate crosslinking. First, MWCNTs-g-PVA was prepared by a radiation-induced "grafting to" method, and its bucky paper was obtained via vacuum filtration. The bucky paper was then immersed in a boric acid solution to form a borate-based linkage between the PVA chains grafted on different MWCNT yarns. Finally, the crosslinked bucky paper was placed on a floating platform as the solar absorber to trigger interfacial water evaporation.

FT-IR spectra of the powders of oxidized MWCNTs and MWCNTs-g-PVA before and after borate crosslinking are shown in Fig. 1a. A strong absorption band located at 1400–1600 cm^{-1} was assigned to the tensile vibration of the graphitic skeleton. The O–H tensile vibration peak at 3366 cm^{-1} and C–O vibration peak at 1285 cm^{-1} appeared in the spectrum of the grafted MWCNT powder, indicating the successful grafting of PVA chains onto MWCNTs after γ-ray irradiation. After borate crosslinking, the intensity of the O–H absorption peak decreased and new absorption peaks appeared. The broad peak around 1430 cm^{-1} was assigned to the stretching vibration of B–O bonds, and the peaks at 1200 cm^{-1} and 1120 cm^{-1} were assigned to the characteristic stretching vibrations of B–O–C bonds [51]. This result proves the formation of polyvinyl borate by the reaction between PVA and boric acid. Figure 1b shows that the oxidized MWCNT powder has a negligible mass loss in the pyrolysis process from 100 °C to 650 °C, while the MWCNTs-g-PVA powder shows two sharp mass loss stages located around 280 °C and 420 °C. This is in accordance with the decomposition behavior of PVA [52], which follows a two-stage mechanism involving the dehydration of PVA (250 to 350 °C) and main chain scission above 380 °C. As for the borate crosslinked MWCNTs-g-PVA, the maximum weight loss temperature of the first stage increased to 338 °C, indicating a better thermal resistance of polyvinyl borate than PVA [51]. The residual weight of the crosslinked MWCNTs-g-PVA after pyrolysis was notably higher than that of the original MWCNTs-g-PVA, demonstrating a high degree of borate crosslinking. The I_D/I_G values from Raman spectra of the oxidized MWCNTs powders and MWCNTs-g-PVA powders before and after borate crosslinking were 1.16, 1.18, and 1.15, respectively (Fig. 1c). This indicates that PVA was grafted onto the walls of the MWCNTs under γ-ray irradiation and some of the grafted PVA chains were regularized by boric acid treatment due to borate formation. Owing to the radiation-induced reduction effect [53], some defects on the graphitic wall of oxidized MWCNTs could be restored by reductive radiolysis species, resulting in a similar density ratio between the D-peak and G-peak. Furthermore, the red-shifted G-band of MWCNTs-g-PVA powders after crosslinking implies that the hydroxyl groups of oxidized MWCNTs are also involved in borate crosslinking, resulting in G-band softening [45]. These results strongly support the success of radiation-induced PVA modification and borate crosslinking of PVA on oxidized MWCNTs.

Figure 2a shows that the bare CA membrane has an absorption in the UV region ascribed to the acetate

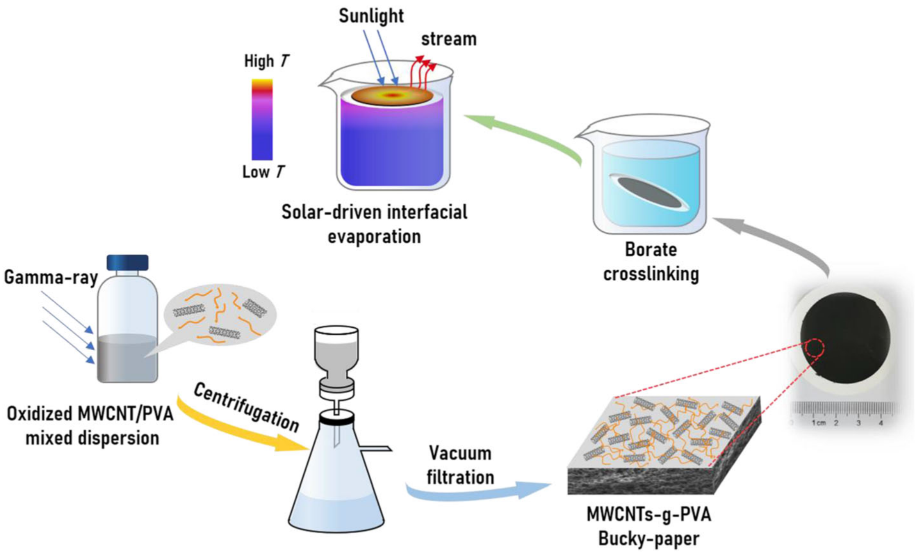

Scheme 1 (Color online) Illustration of the fabrication of crosslinked MWCNT bucky paper for solar-driven interfacial water evaporation

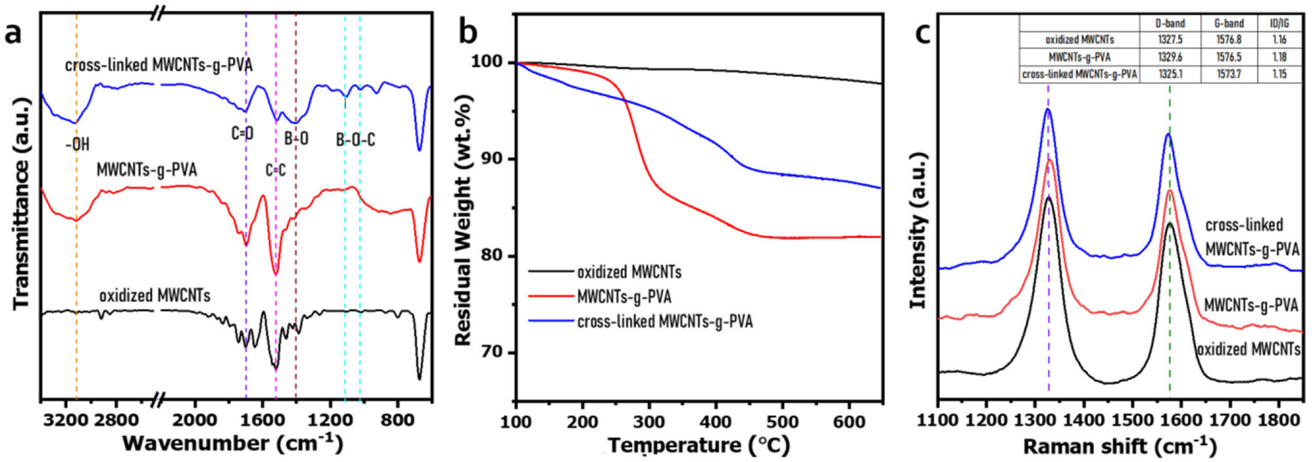

Fig. 1 (Color online) **a** FT-IR spectra, **b** TG curves, and **c** Raman spectra of the oxidized MWCNT powders and MWCNTs-g-PVA powders before and after borate crosslinking

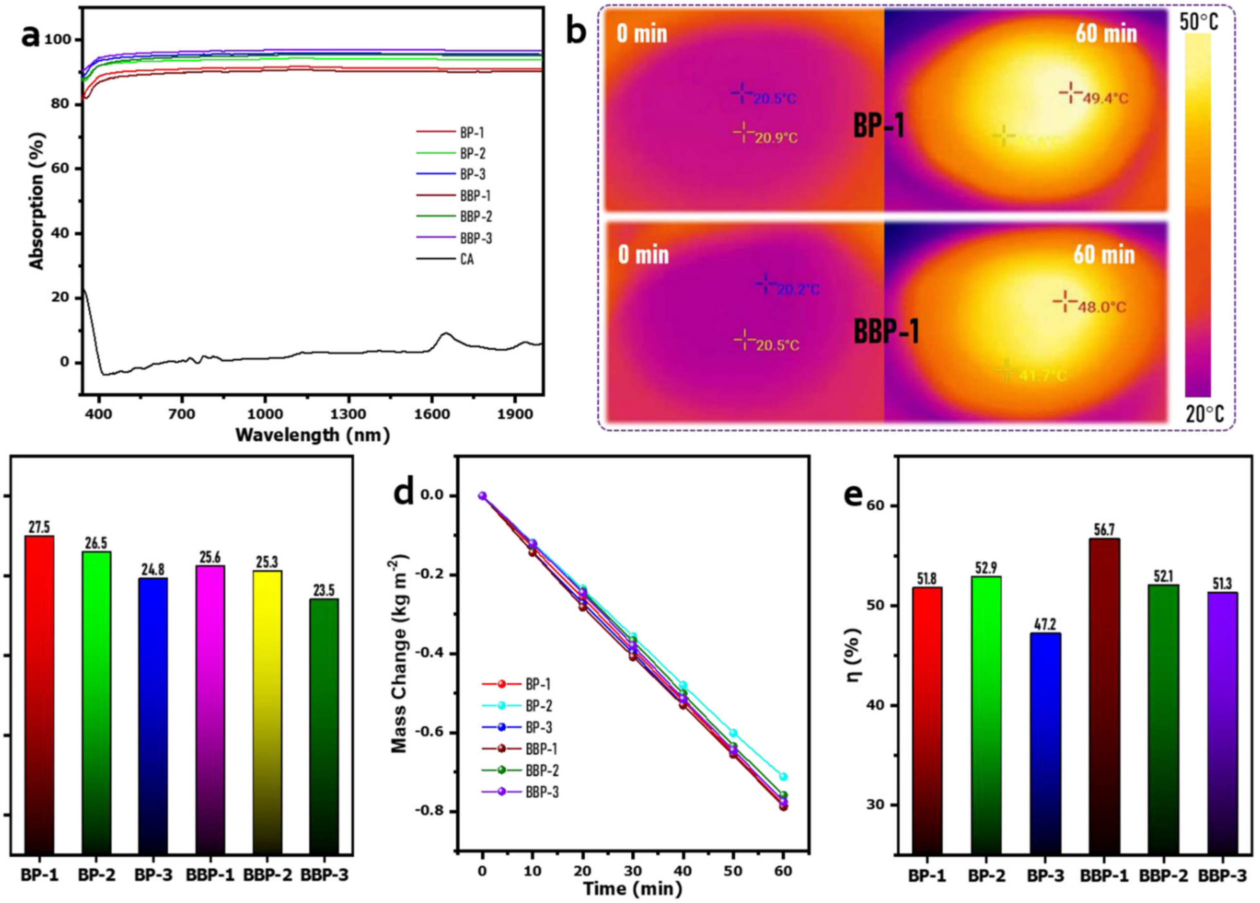

Fig. 2 (Color online) **a** UV–vis-NIR absorption spectra of the BP membranes with different thicknesses before and after borate crosslinking; **b** thermal infrared images of BP-1 and BBP-1 membranes before and after 1 h of 1 sun illumination; **c** surface temperature changes of different BP and BBP membranes before and after 1 sun illumination; **d** solar evaporation rates of different BP and BBP membranes; **e** efficiencies of the BP and BBP membranes over time of 1 sun illumination in deionized water

absorption around 270 nm [54] but allows the strong transmission of visible and NIR light. The absorbances of all BP and BBP membranes across the UV–VIS-NIR region reached more than 85%, and considerably increased with the increase in MWCNTs-g-PVA loading. The absorbance difference between the BP and BBP membranes is very small, indicating the insignificant effect of borate crosslinking of PVA on the solar light absorption. The thermal infrared images of BP-1 and BBP-1 membranes both exhibited an almost identical temperature rise after 1 h illumination of 1 sun, proving that the photothermal conversion of all BP and BBP membranes is not affected by boric acid crosslinking. The temperature of BP-1 membrane increased from 20.5 °C to 49.4 °C, while that of BBP-1 membrane increased from 20.2 °C to 48 °C (Fig. 2b). The BP and BBP membranes were placed on a floating platform and illuminated with 1 sun. The average surface temperature increase and water loss rate (i.e., evaporation rate) were recorded and are shown in Figs. 2c, d. The temperature rise was inversely proportional to the thickness, with a temperature rise of 27.5 °C for BP-1 and 24.8 °C for BP-3. The same trend was also observed for the BBP membranes, but the temperature rise of the BBP membranes was lower than those of the corresponding BP membranes (Fig. 2c). However, all the BP and BBP membranes in deionized water under 1 sun illumination demonstrated an evaporation rate of approximately 0.8 kg m^{-2} h^{-1} with no obvious dependence on either the loading of MWCNTs-g-PVA or the borate crosslinking (Fig. 2d). The solar evaporation efficiencies were calculated according to the evaporation rates and the photothermal induced surface temperature changes, which are shown in Fig. 2e. The BBP-1 membrane achieved the maximum evaporation rate at a low temperature; consequently, its conversion efficiency was the best. In addition, the data demonstrate that increasing the mass of MWCNTs-g-PVA on membranes can increase the light absorption but cannot improve the water evaporation rate or efficiency directly. This is because the light-to-heat conversion ability is determined by the intrinsic optical performance and texture structure of the photothermal materials. Although the overloading of MWCNTs-g-PVA yarns can improve the light absorption capacity of the membrane, it also leads to a decrease in the surface porosity of the membranes [49]. This in turn increases the light reflectance, reduces the light energy utilization, and restricts the water transport owing to the decreasing capillary action [55], eventually resulting in a low evaporation efficiency.

As BP-1 and BBP-1 samples showed better performances in the solar-driven interfacial evaporation test, they were used as the main samples for subsequent tests. Figure 3a shows the evaporation rate of the BBP-1 membrane under different light intensities. Evaporation rates of 0.44, 0.79, 1.26, and 2.17 kg m^{-2} h^{-1} were obtained from the illumination of 0.5, 1, 1.5, and 2 sun, respectively. The surface properties of the membranes were studied by water contact angle analysis. As shown in Fig. 3b, the BP-1 membrane showed good hydrophilicity ($\sim$ 30°) due to the grafting of hydrophilic PVA chains. The water contact angle increased after borate crosslinking (BBP-1 membrane), indicating that the hydrophilicity decreased because the hydroxyl groups of PVA were consumed to form borate crosslinks. The hydrophilicity of the BBP-1 membrane increased after solar illumination, which could be attributed to the rearrangement of the surface groups during the photothermal process.

Figure 4a, b shows that the color of the BP membranes faded after 1 h of interfacial evaporation in water under 1 sun illumination, especially for the BP-1 membrane. The MWCNTs-g-PVA layer (bucky paper) on the BP membranes was completely swollen after solar-driven evaporation and easily abrased (see the inset in Fig. 4b), indicating their poor water resistance and mechanical durability after solar irradiation. PVA is prone to dissolving in water at high temperatures. Figure 2b shows that the surface temperature of BP membranes is up to 49.4 °C under 1 sun illumination, which causes significant hydration of the PVA chains grafted on oxidized MWCNT yarns and the extreme swelling of the bucky paper. It also demonstrates that the linkage between grafted MWCNT yarns is not sufficient to resist water swelling under simulated sunlight illumination. In contrast, the BBP membranes showed almost no color change (Fig. 4c, d) and were not easily abrased after solar-driven evaporation (see the inset in Fig. 4d). This is because the covalent B $-$ O $-$ C bond formed in the borate-PVA crosslinking network structure has a stronger heat resistance than the hydrogen bonding between the hydroxyl group of PVA and oxidized MWCNTs. Therefore, the BBP membranes have stronger water resistances at high temperatures than the BP membranes. For further confirmation, we placed the BP-1 and BBP-1 membranes in hot water (70 °C) for 30 min and then scratched the membranes with steel sharp-nosed tweezers (Fig. S1). The CNT layer on the BP-1 membrane was easily damaged, while that on the BBP-1 membrane exhibited a mechanical resistance, indicating that borate crosslinking improved the water resistance of the BBP membrane.

To further confirm this, micromorphological changes of the BP-1 and BBP-1 membranes before and after solar-driven interfacial water evaporation were investigated by SEM of the surfaces and cross sections (Figs. 5, 6). The MWCNTs-g-PVA yarns were uniformly deposited (Fig. 5a), and a new porous skin layer was formed on the surface of the CA substrate (Fig. 6a). Figure 5b shows that many bulges and aggregates appear on the surface of the BP-1 membrane, and the surface pores of the CA substrate are revealed after solar-driven interfacial water evaporation owing to water swelling and yarn loss. The BBP-1 membrane exhibited no obvious surface changes in the micromorphology before and after solar-driven interfacial

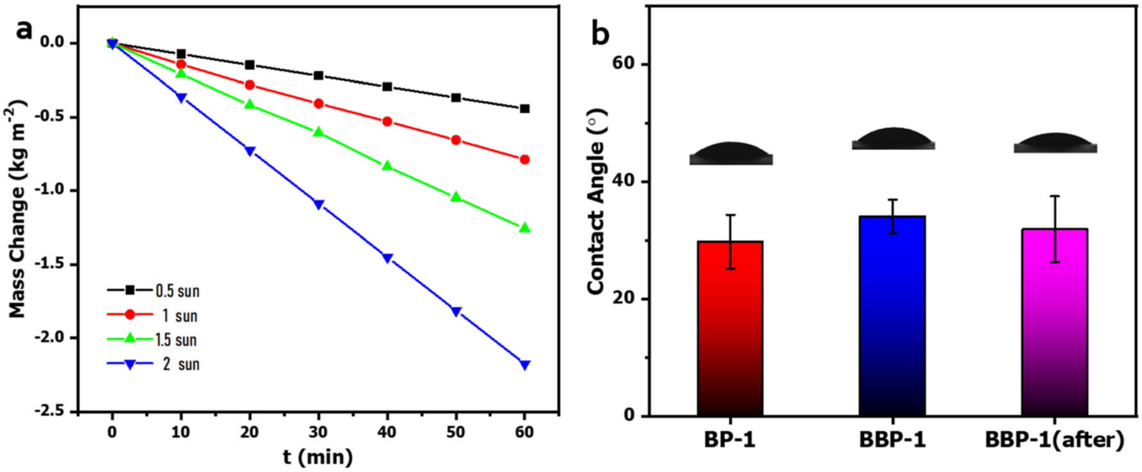

Fig. 3 (Color online) **a** Solar evaporation rates of BBP-1 membranes in deionized water over time under 0.5, 1, 1.5, and 2 sun illumination; **b** water contact angle of the BP-1 membrane, and the BBP-1 membrane before and after solar-driven interfacial evaporation

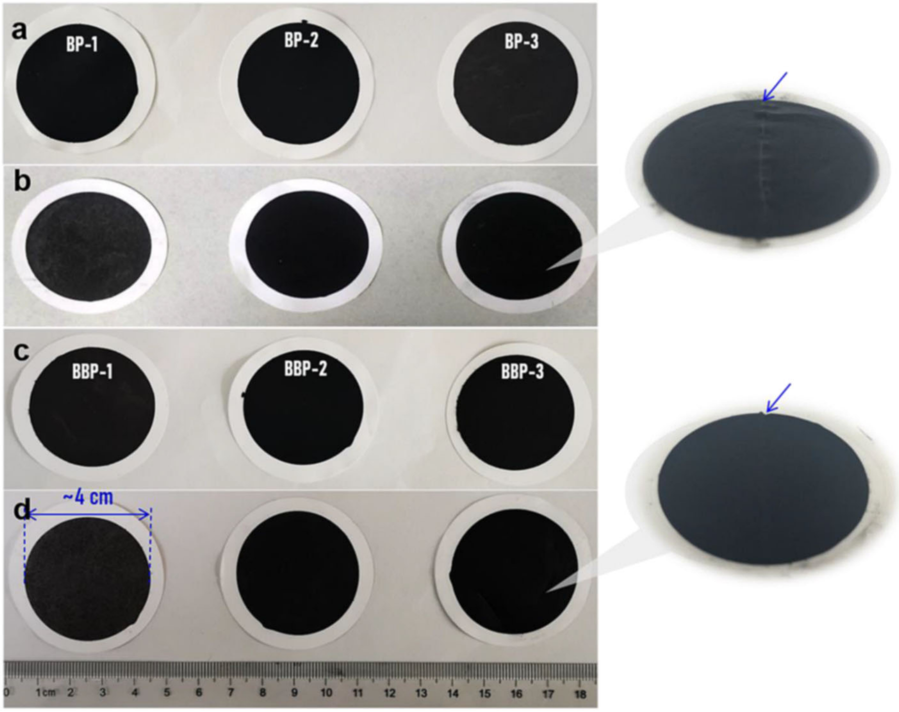

Fig. 4 Digital images of BP and BBP membranes before (**a**, **c**) and after (**b**, **d**) interfacial evaporation in water under 1 sun illumination. Inserts in **b** and **d** are the digital images of mechanical scratch testing of BP-3 and BBP-3 membranes after interfacial evaporation

evaporation (Fig. 5c, d). SEM images of the cross section confirm that the MWCNTs-g-PVA layer on the BP-1 membrane was damaged by interfacial water evaporation (Fig. 6a, b) and that of the BBP-1 membrane retained the same porous and intact structure that it had before solar illumination (Fig. 6c, d). Therefore, SEM observations of the surface and cross section of the membranes demonstrate that the borate crosslinking treatment effectively enhanced the mechanical durability of the MWCNT bucky paper membranes and endowed them with good tolerance to the solar-driven interfacial water evaporation process. BBP-1 and BBP-2 bucky paper samples were very thin owing to the low loading capacity, and some MWCNTs-g-PVA yarns were embedded into the CA membrane, as shown in the SEM image (Fig. 6). Therefore, the thickness of the surface layer was not easy to distinguish. However, the BBP-3 sample could be easily tested and possessed a thickness of approximately 1.5 μm (Fig. S2), implying an increase in the membrane thickness with an increase in the loading capacity of MWCNTs-g-PVA.

To assess the durability of the BBP membranes, the BBP-1 membrane was used to treat salt solutions with different salinities as well as strongly acidic solutions via a solar-driven interfacial evaporation process (Fig. 7a). As

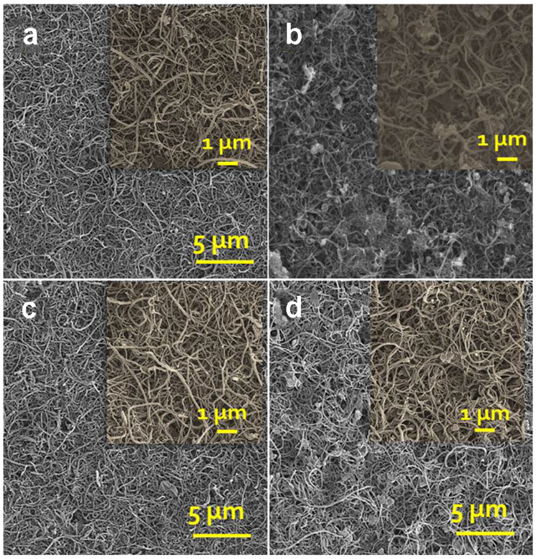

Fig. 5 (Color online) Surface micromorphologies of BP-1 membrane **a** before and **b** after solar-driven interfacial water evaporation in water and those of BBP-1 membrane **c** before and **d** after solar-driven interfacial water evaporation in water

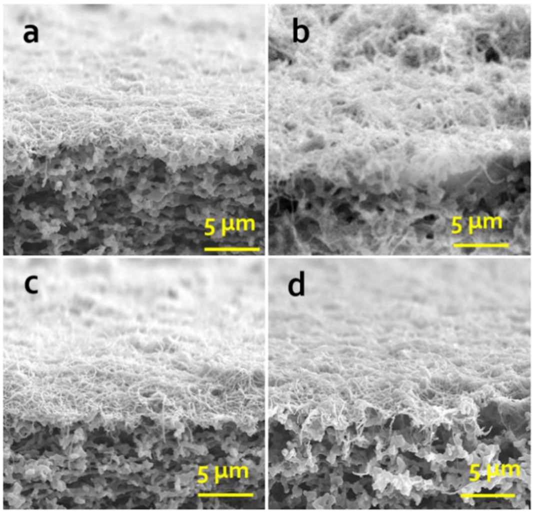

Fig. 6 (Color online) Cross-section micromorphologies of BP-1 membrane **a** before and **b** after solar-driven interfacial water evaporation in water and those of BBP-1 membrane **c** before and **d** after solar-driven interfacial water evaporation in water

expected, the temperature increases exceeded those in deionized water at 3–6 °C (Fig. 7b). A water evaporation rate of 0.76 kg m^{-2} h^{-1} was achieved in both 3.5 wt% NaCl solution and sulfuric acid solution (Fig. 7c). This value is very close to that in deionized water (0.79 kg m^{-2} h^{-1}), indicating that the evaporation capacity of BBP membranes is very stable even in the treatment of seawater and acidic solutions. Additionally, the evaporation efficiencies of the BBP-1 membrane in the 3.5 wt% NaCl solution and sulfuric acid solution were 54% and 51.6%, respectively (Fig. 7d), which were also comparable to efficiencies of BBP-1 membrane in deionized water (56%). In the NaCl solution, owing to the abundant and strong electrostatic attraction between water molecules and ions (Na^+ and Cl^-), the freedom of motion of water molecules inevitably decreases with the increasing NaCl concentration in solution. Therefore, the boiling point of salt water is always higher than that of pure water. As a consequence, the evaporation rate and efficiency of salt water decrease with the increase in the brine concentration. Similarly, the evaporation efficiency of the sulfuric acid solution was lower than that of pure water. Unexpectedly, the evaporation rate in saturated brine was still relatively high at 0.70 kg m^{-2} h^{-1} (Fig. 7c), just 10% lower than that in deionized water (0.79 kg m^{-2} h^{-1}). This finding indicates that the BBP membranes have good applicability for the desalination of salt water by solar-driven interfacial evaporation, even for the treatment of saturated salt solutions, which has not been reported so far in the literature.

Solar-driven interfacial water evaporation has been greatly valued in water desalination in recent years because of its high efficiency and environmental friendliness, with many efforts made to improve the evaporation rate and energy efficiency [56, 57]. However, the salt accumulation on the surface of the solar absorber, resulting from the water evaporation at the air–water interface and the slow diffusion of water back through the transport channels, is still a key challenge for its practical application. The salt accumulation on the solar absorber not only reduces its light absorption but also blocks water transport [58]. This results in a significant decrease in the evaporation efficiency over time and lowers the long-term stability of solar evaporation systems [59], especially in high-salinity environments [60]. Unfortunately, most of the reported solar evaporators have focused on seawater (3.5% salinity), while solar evaporators for high-salinity brine ($\geq$ 10%) have not received sufficient attention [60]. The high-saline solutions could be present in industrial production environments and wastewater treatments. To confirm the evaporation durability of the BBP membranes in a saturated NaCl solution, a long-term continuous solar evaporation test was performed under 1 sun illumination. Figure 8a shows that the mass loss of the saturated NaCl solution linearly increases with the illumination time, which reflects an almost constant evaporation rate in saturated NaCl solution during the continuous 5 h of test time (Fig. 8b). Figure 8c shows an increasing number of white salt crystals precipitating on the BBP-1 membrane surface with the increasing evaporation time, which is evidence of water evaporation from the saturated NaCl solution. Although salt readily accumulated on the BBP-1 membrane surface, the solar evaporation performance in saturated NaCl solution remained at a stable level over a long

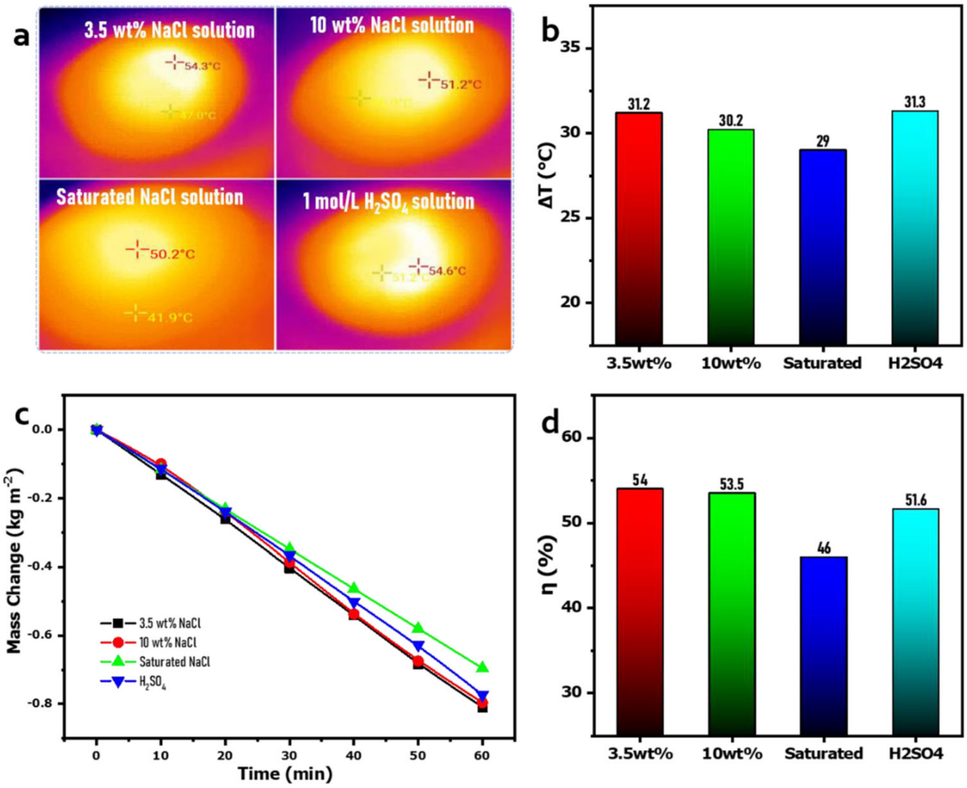

Fig. 7 (Color online) **a** Thermal infrared images, **b** temperature changes, **c** solar evaporation rates, and **d** evaporation efficiencies of BBP-1 membrane under 1 sun illumination in 3.5 wt% NaCl solution, 10 wt% NaCl solution, saturated NaCl solution, and 1 mol L^{-1} H_2SO_4 solution

test time. This indicates the long-term stability of the BBP-1 membrane for the evaporation treatment of high-salinity brine. In other words, the salt that accumulated on the surface of the BBP-1 membrane did not significantly hinder the absorption of incident light or the supply of water. This could be attributed to the excellent hydrophilic, porous, and hierarchical surface structure, high solar absorption of the BBP membranes, and unique water molecule transport behavior of the CNT yarns. Water molecules can be transported through the interior channel of CNTs in contact with a reservoir of aqueous solution [61], but dissolved ions in solution are blocked by size constraints and cation–π interactions [62]. The PVA/CNT hybrid was also confirmed to possess fast water transport because of the efficient interior infiltration and PVA decoration of the cellular structures of CNTs [63]. Furthermore, the grafted PVA chains on oxidized MWCNTs can greatly facilitate water evaporation owing to the reduced water evaporation enthalpy in the hydrogel network [64]. In other words, water can be transported to the BBP-1 membrane surface without the interference of the salt scale. Therefore, the evaporation rate of the BBP membranes is quite stable during the continuous long-term solar evaporation of high-salinity water. To further illustrate the possibility of BBP-1 membrane treating seawater for a long time, 7-day continuous solar evaporation tests in 3.5% NaCl solution were carried out under outdoor sunlight conditions. Figure 8d shows that the evaporation rate of the membrane did not decrease significantly over the duration. There was no obvious precipitation of salt on the membrane surface (Fig. 8e), indicating that the membrane has long-term stability in seawater treatment. Additionally, the salt accumulated on the membrane surface can be ablated rapidly in water (Video S1). The washed membrane also shows an evaporation rate ($\sim$ 0.7 kg m^{-2} h^{-1}) similar to the initial membrane, further indicating the stability of BBP membranes. The BBP-1 membrane also exhibited no damage and a stable evaporation rate and efficiency after solar evaporation in 1 mol L^{-1} H_2SO_4 solution with irradiation of 1 sun (Fig. 7c–d). This result substantiates the good chemical resistances of these membranes to high salt and strong acidic conditions. Finally, we compared the evaporation performance of BBP membranes with other recently reported photothermal materials for solar-driven interfacial evaporation [65–68]. As a comparison, although the evaporation rate of the BBP membrane is lower than those reported in the literature, the evaporation stability during continuous long-term processes in high-salinity water is still undoubtedly exciting.

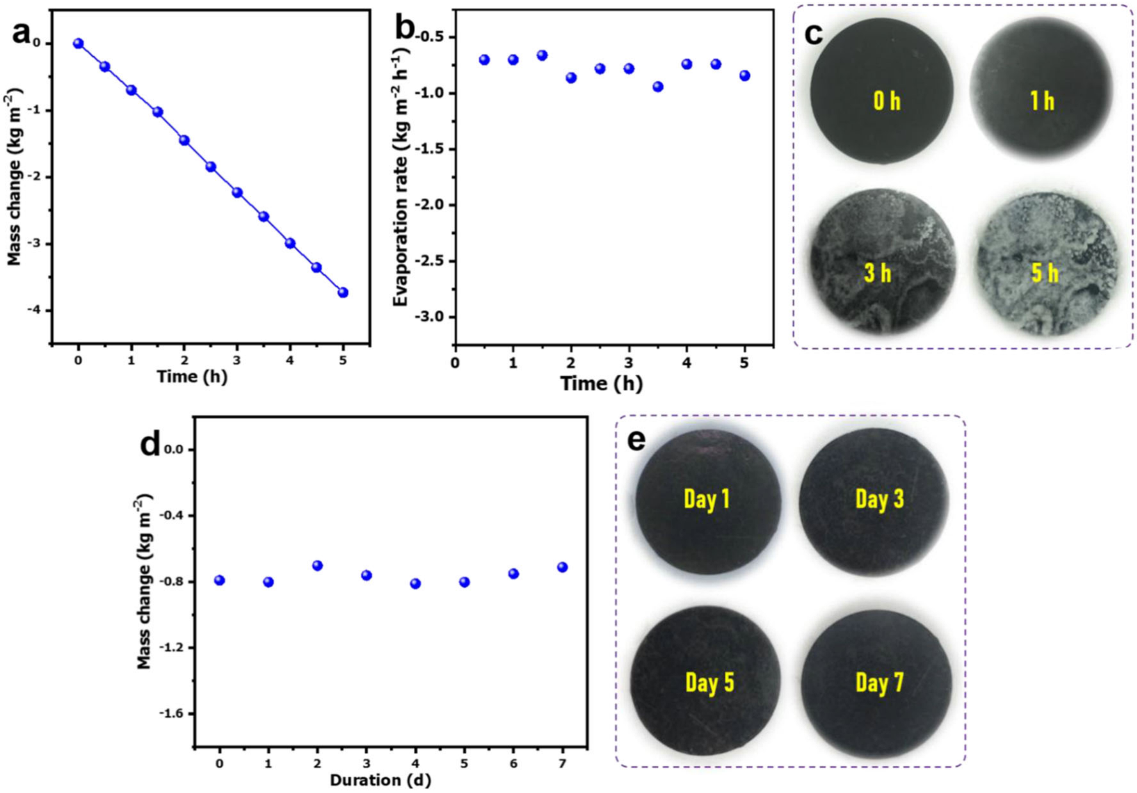

Fig. 8 (Color online) Long-term continuous solar evaporation test of BBP-1 membrane under 1 sun illumination in saturated NaCl solution: **a** Mass change of saturated NaCl solution; **b** average solar evaporation rates; **c** salt accumulation on BBP-1 membrane surface over test time. Seven-day continuous solar evaporation test of the BBP-1 membrane under natural light in 3.5% NaCl solution: **d** Mass change of 3.5% NaCl solution; **e** surface morphological change of BBP-1 membrane over time

4 Conclusion

In summary, a durable MWCNT bucky paper was built by radiation-induced grafting of PVA to oxidized MWCNT yarns with subsequent crosslinking with boric acid. The micromorphological investigation via SEM demonstrated that the obtained BBP membranes could withstand hot water swelling and maintain their porous and continuous architecture after solar-driven interfacial water evaporation. The BPP membranes exhibited an evaporation rate of 0.79 kg m^{-2} h^{-1} and an evaporation efficiency of 56.8%. Furthermore, the BBP membranes that were used to treat saline and acidic solutions had comparable solar evaporation rates. The good chemical resistances to high salt and strong acidic conditions and the excellent salt-blocking properties of the BPP membranes originate from the ultrafast water transport and the unique ion-blocking effects in the interior channel of the CNTs. These results indicate the impressive suitability of the BBP membranes for the solar evaporation of saline and strong acidic solutions. The most important finding is that the evaporation rate and efficiency of the BBP-1 membrane exhibited no significant reduction during the continuous long-term evaporation of the saturated NaCl solution, even with severe salt accumulation on the BBP-1 membrane surface. This demonstrates the excellent durability and long-term stability of these membranes for the high-salinity water treatment. In summary, this study demonstrates a facile solution process to construct durable MWCNT bucky paper for water treatment via solar-induced interfacial water evaporation, which would inspire other studies on functional nanocarbon materials.

Supplementary Information The online version contains supplementary material available at https://doi.org/10.1007/s41365-021-00978-9.

Acknowledgements The authors cordially thank Prof. Lin-Fan Li and his group from Shanghai Institute of Applied Physics for their enthusiastic helps and supports to the irradiation treatment. They also sincerely appreciate the supports from Shanghai Engineering Research Centre of Green Energy Chemical Engineering.

Author contributions All authors contributed to the study conception and design. Material preparation, data collection and analysis were performed by Yu-Qing Qiao, Yu Gu and Bo-Wu Zhang. The first draft of the manuscript was written by Yu-Qing Qiao and Yu Gu, and all authors commented on previous versions of the manuscript. All authors read and approved the final manuscript.

References

1. H. Manchanda, M. Kumar, Study of water desalination techniques and a review on active solar distillation methods. Environ. Prog. Sustain. Energ. **37**, 444–464 (2018). https://doi.org/10.1002/ep.12657
2. T. Ding, Y. Zhou, W.L. Ong et al., Hybrid solar-driven interfacial evaporation systems: Beyond water production towards high solar energy utilization. Mater. Today **42**, 178–191 (2021). https://doi.org/10.1016/j.mattod.2020.10.022
3. N. Li, L. Qiao, J. He et al., Solar-driven interfacial evaporation and self-powered water wave detection based on an all-cellulose monolithic design. Adv. Func. Mater. **31**, 2008681 (2021). https://doi.org/10.1002/adfm.202008681
4. X. Wu, G.Y. Chen, G. Owens et al., Photothermal materials: a key platform enabling highly efficient water evaporation driven by solar energy. Mater. Today Energ. **12**, 277–296 (2019). https://doi.org/10.1016/j.mtener.2019.02.001
5. J. Chen, Z. Ye, F. Yang et al., Plasmonic nanostructures for photothermal conversion. Small Sci. **1**, 2000055 (2021). https://doi.org/10.1002/smsc.202000055
6. Y. Lin, H. Xu, X. Shan et al., Solar steam generation based on the photothermal effect: from designs to applications, and beyond. J. Mater. Chem. A. **7**, 19203–19227 (2019). https://doi.org/10.1039/C9TA05935K
7. Z. Deng, J. Zhou, L. Miao et al., The emergence of solar thermal utilization: solar-driven steam generation. J. Mater. Chem. A. **5**, 7691–7709 (2017). https://doi.org/10.1039/C7TA01361B
8. F. Liu, Y. Lai, B. Zhao et al., Photothermal materials for efficient solar powered steam generation. Front. Chem. Sci. Eng. **13**, 636–653 (2019). https://doi.org/10.1007/s11705-019-1824-1
9. C. Chen, Y. Kuang, L. Hu, Challenges and opportunities for solar evaporation. Joule **3**, 683–718 (2019). https://doi.org/10.1016/j.joule.2018.12.023
10. Y. Shi, R. Li, Y. Jin et al., A 3D photothermal structure toward improved energy efficiency in solar steam generation. Joule **2**, 1171–1186 (2018). https://doi.org/10.1016/j.joule.2018.03.013
11. D. Huang, J. Zhang, G. Wu et al., A solar evaporator based on hollow polydopamine nanotubes with all-in-one synergic design for highly-efficient water purification. J. Mater. Chem. A **9**, 15776–15786 (2021). https://doi.org/10.1039/D1TA03335B
12. W. Guan, Y. Guo, G. Yu, Carbon materials for solar water evaporation and desalination. Small 2007176 (2021). https://doi.org/10.1002/smll.202007176
13. P. He, L. Hao, N. Liu et al., Controllable synthesis of sea urchin-like carbon from metal-organic frameworks for advanced solar vapor generators. Chem. Eng. J. **423**, 130268 (2021). https://doi.org/10.1016/j.cej.2021.130268
14. D.P. Storer, J.L. Phelps, X. Wu et al., Graphene and rice-straw-fiber-based 3D photothermal aerogels for highly efficient solar evaporation. ACS Appl Mater Interf. **12**, 15279–15287 (2020). https://doi.org/10.1021/acsami.0c01707
15. Z. Hu, L. Hao, N. Liu et al., High-performance bilayer solar evaporators constructed by candle-derived carbon nanoparticle/wood hybrid. Materials Today Commun. **28**, 102636 (2021). https://doi.org/10.1016/j.mtcomm.2021.102636
16. S. Fallah, H.R. Mamaghani, R. Yegani et al., Use of graphene substrates for wastewater treatment of textile industries. Adv. Compos. Hybrid Mater. **3**, 187–193 (2020). https://doi.org/10.1007/s42114-020-00146-4
17. C. Liu, Y. Lin, Y. Dong et al., Fabrication and investigation on Ag nanowires/TiO2 nanosheets/graphene hybrid nanocomposite and its water treatment performance. Adv. Compos. Hybrid Mater. 1–13 (2020). https://doi.org/10.1007/s42114-020-00164-2
18. Y. Zhang, J. Guo, G. Han et al., Molecularly soldered covalent organic frameworks for ultrafast precision sieving. Sci Adv. **7**, eabe8706 (2021). https://doi.org/10.1126/sciadv.abe8706
19. Y. Zhang, X. Cheng, X. Jiang et al., Robust natural nanocomposites realizing unprecedented ultrafast precise molecular separations. Mater. Today **36**, 40–47 (2020). https://doi.org/10.1016/j.mattod.2020.02.002
20. L. Li, Zang L., Zhang S., et al. GO/CNT-silica Janus nanofibrous membrane for solar-driven interfacial steam generation and desalination. J. Taiwan Inst. Chem. Eng. **111**, 191–197 (2020). https://doi.org/10.1016/j.jtice.2020.03.015
21. M.H.O. Rashid, S.F. Ralph, Carbon nanotube membranes: synthesis, properties, and future filtration applications. Nanomaterials **7**, 99 (2017). https://doi.org/10.3390/nano7050099
22. G.S. Simate, S.E. Iyuke, S. Ndlovu et al., Human health effects of residual carbon nanotubes and traditional water treatment chemicals in drinking water. Environ. Int. **39**, 38–49 (2012). https://doi.org/10.1016/j.envint.2011.09.006
23. Y. Liu, Y. Zhao, B. Sun et al., Understanding the toxicity of carbon nanotubes. Acc. Chem. Res. **46**, 702–713 (2013). https://doi.org/10.1021/ar300028m
24. Y. Rodriguez-Yañez, B. Muñoz, A. Albores, Mechanisms of toxicity by carbon nanotubes. Toxicol. Mech. Methods **23**, 178–195 (2013). https://doi.org/10.3109/15376516.2012.754534
25. J. Dong, Q. Ma, Advances in mechanisms and signaling pathways of carbon nanotube toxicity. Nanotoxicology **9**, 658–676 (2015). https://doi.org/10.3109/17435390.2015.1009187
26. C. Corredor, W.C. Hou, S.A. Klein et al., Disruption of model cell membranes by carbon nanotubes. Carbon **60**, 67–75 (2013). https://doi.org/10.1016/j.carbon.2013.03.057
27. C.J. Frizzell, M. in het Panhuis, D.H. Coutinho et al., Reinforcement of macroscopic carbon nanotube structures by polymer intercalation: the role of polymer molecular weight and chain conformation. Phys. Rev. B **72**, 245420 (2005). https://doi.org/10.1103/PhysRevB.72.245420
28. Q. Liu, M. Li, Z. Wang et al., Improvement on the tensile performance of buckypaper using a novel dispersant and functionalized carbon nanotubes. Compos. Part A Appl. Sci. Manuf. **55**, 102–109 (2013). https://doi.org/10.1016/j.compositesa.2013.08.011
29. M.J. Yee, N.M. Mubarak, M. Khalid et al., Synthesis of polyvinyl alcohol (PVA) infiltrated MWCNTs buckypaper for strain sensing application. Sci. Rep. **8**, 17295 (2018). https://doi.org/10.1038/s41598-018-35638-3
30. S. Cosnier, R. Haddad, D. Moatsou et al., Biofunctionalizable flexible bucky paper by combination of multi-walled carbon nanotubes and polynorbornene-pyrene—application to the bioelectrocatalytic reduction of oxygen. Carbon **93**, 713–718 (2015). https://doi.org/10.1016/j.carbon.2015.05.099
31. W.A.D. Wan Dalina, M. Mariatti, S.H. Tan, Multi-walled carbon nanotubes buckypaper/epoxy composites: effect of loading and pressure on tensile and electrical properties. Poly. Bull. **76**, 2801–2817 (2019). https://doi.org/10.1007/s00289-018-2530-8
32. A. Alshahrani, A. Alharbi, S. Alnasser et al., Enhanced heavy metals removal by a novel carbon nanotubes buckypaper membrane containing a mixture of two biopolymers: Chitosan and i-carrageenan. Separat. Purif. Technol. **276**, 119300 (2021). https://doi.org/10.1016/j.seppur.2021.119300
33. A. Satti, A. Perret, J.E. McCarthy et al., Covalent crosslinking of single-walled carbon nanotubes with poly(allylamine) to produce mechanically robust composites. J. Mater. Chem. **20**, 7941–7943 (2010). https://doi.org/10.1039/C0JM01515F
34. D.N. Ventura, R.A. Stone, K.S. Chen et al., Assembly of cross-linked multi-walled carbon nanotube mats. Carbon **48**, 987–994 (2010). https://doi.org/10.1016/j.carbon.2009.11.016

35. A.G. Chmielewski, M. Haji-Saeid, Radiation technologies: past, present and future. Radiation Phys. Chem. **71**, 17–21 (2004). https://doi.org/10.1016/j.radphyschem.2004.05.040
36. K. Čubová, V. Čuba, Synthesis of inorganic nanoparticles by ionizing radiation—a review. Radiation Phys. Chem. **169**, 108774 (2020). https://doi.org/10.1016/j.radphyschem.2020.108774
37. Y. Gu, Y. Qiao, Y. Meng et al., One-step synthesis of well-dispersed polypyrrole copolymers under gamma-ray irradiation. Polym. Chem. **12**, 645–649 (2021). https://doi.org/10.1039/D0PY01566K
38. Y. Wang, M. Xie, J. Lan et al., Radiation controllable synthesis of robust covalent organic framework conjugates for efficient dynamic column extraction of $99TcO_4^-$. Chem. **6**, 2796–2809 (2020). https://doi.org/10.1016/j.chempr.2020.08.005
39. X. Ding, M. Yu, X. Zheng et al., Stability study of disperse blue 79 under ionizing radiation. Nucl. Sci. Tech. **31**, 21 (2020). https://doi.org/10.1007/s41365-020-0724-x
40. Y. Gu, B.W. Zhang, Z. Guo et al., Radiation-induced crosslinking: a novel avenue to permanent 3D modification of polymeric membranes. Nucl. Sci. Tech. **32**, 70 (2021). https://doi.org/10.1007/s41365-021-00905-y
41. B. Zhang, L. Liu, S. Xie et al., Built-up superhydrophobic composite membrane with carbon nanotubes for water desalination. RSC Adv. **4**, 16561–16566 (2014). https://doi.org/10.1039/C3RA47436D
42. F. Cataldo, On the action of γ radiation on solid C60 and C70 fullerenes: a comparison with graphite irradiation. Fullerene Scie. Technol. **8**, 577–593 (2000). https://doi.org/10.1080/10641220009351435
43. M.C. Evora, D. Klosterman, K. Lafdi et al., Functionalization of carbon nanofibers through electron beam irradiation. Carbon **48**, 2037–2046 (2010). https://doi.org/10.1016/j.carbon.2010.02.012
44. J. Ye, B. Zhang, Y. Gu et al., Tailored graphene oxide membranes for the separation of ions and molecules. ACS Appl. Nano Mat. **2**, 6611–6621 (2019). https://doi.org/10.1021/acsanm.9b01356
45. Y. Gu, J. Zhao, H. Zhou et al., Crosslinking imidazolium-intercalated GO membrane for acid recovery from low concentration solution. Carbon 183, 830–839 (2021). https://doi.org/10.1016/j.carbon.2021.07.050
46. C. Yu, B. Zhang, F. Yan et al., Engineering nano-porous graphene oxide by hydroxyl radicals. Carbon **105**, 291–296 (2016). https://doi.org/10.1016/j.carbon.2016.04.050
47. Y. Gu, B. Zhang, Z. Fu et al., Poly (vinyl alcohol) modification of poly(vinylidene fluoride) microfiltration membranes for oil/water emulsion separation via an unconventional radiation method. J. Memb. Sci. **619**, 118792 (2021). https://doi.org/10.1016/j.memsci.2020.118792
48. Y. Gu, J. Zhao, H. Zhou et al., Engineering robust RGO/PVA composite membrane for acid recovery via electron beam irradiation. Carbon (2022). https://doi.org/10.1016/j.carbon.2021.11.035
49. Y. Gu, H. Li, L. Liu et al., Constructing CNTs-based composite membranes for oil/water emulsion separation via radiation-induced "grafting to" strategy. Carbon **178**, 678–687 (2021). https://doi.org/10.1016/j.carbon.2021.03.051
50. B. Zhang, S. Xie, R. Wei et al., Radiation induced graft polymerization of multi-walled carbon nanotubes for superhydrophobic composite membrane preparation. Sci. China Chem. **59**, 303–309 (2016). https://doi.org/10.1007/s11426-015-5472-0
51. O. Koysuren, M. Karaman, H. Dinc, Preparation and characterization of polyvinyl borate/polyvinyl alcohol (PVB/PVA) blend nanofibers. J. Appl. Poly. Sci. **124**, 2736–2741 (2012). https://doi.org/10.1002/app.35035
52. Y. Park, M. You, J. Shin et al., Thermal conductivity enhancement in electrospun poly(vinyl alcohol) and poly(vinyl alcohol)/cellulose nanocrystal composite nanofibers. Sci. Rep. **9**, 3026 (2019). https://doi.org/10.1038/s41598-019-39825-8
53. B. Zhang, L. Li, Z. Wang et al., Radiation induced reduction: an effective and clean route to synthesize functionalized graphene. J. Mater. Chem. **22**, 7775–7781 (2012)
54. A. Bos, The UV spectra of cellulose and some model compounds. J. Appl. Poly. Sci. **16**, 2567–2576 (1972). https://doi.org/10.1002/app.1972.070161010
55. Y. Li, W. Hong, H. Li et al., Solar absorber with tunable porosity to control the water supply velocity to accelerate water evaporation. Desalination **511**, 115113 (2021). https://doi.org/10.1016/j.desal.2021.115113
56. L. Zhu, M. Gao, C.K.N Peh et al., Recent progress in solar-driven interfacial water evaporation: Advanced designs and applications. Nano Energy **57**, 507–518 (2019). https://doi.org/10.1016/j.nanoen.2018.12.046
57. Z. Xu, Z. Li, Y. Jiang et al., Recent advances in solar-driven evaporation systems. J. Materials Chem. A **8**, 25571–25600 (2020). https://doi.org/10.1039/D0TA08869B
58. G. Liu, T. Chen, J. Xu et al., Salt-rejecting solar interfacial evaporation. Cell Rep. Phys. Sci. **2**, 100310 (2021). https://doi.org/10.1016/j.xcrp.2020.100310
59. K. Xu, C. Wang, Z. Li et al., Salt mitigation strategies of solar-driven interfacial desalination. Adv. Func. Mater. **31**, 2007855 (2021). https://doi.org/10.1002/adfm.202007855
60. Q. Huang, C. Du, C. Guo et al., A high-efficiency salt-rejecting solar evaporator with optimized porous structure for continuous solar desalination. Appl. Thermal Eng. **187**, 116515 (2021). https://doi.org/10.1016/j.applthermaleng.2020.116515
61. A. Berezhkovskii, G. Hummer, Single-file transport of water molecules through a carbon nanotube. Phys. Rev. Lett. **89**, 064503 (2002). https://doi.org/10.1103/PhysRevLett.89.064503
62. G. Shi, J. Liu, C. Wang et al., Ion enrichment on the hydrophobic carbon-based surface in aqueous salt solutions due to cation-π interactions. Sci. Rep. **3**, 3436 (2013). https://doi.org/10.1038/srep03436
63. L. Zhao, J. Zhang, P. Cao et al., Fast water transport reversible CNT/PVA hybrid hydrogels with highly environmental tolerance for multifunctional sport headband. Compos. Part B Eng. **211**, 108661 (2021). https://doi.org/10.1016/j.compositesb.2021.108661
64. X. Zhou, F. Zhao, Y. Guo et al., A hydrogel-based antifouling solar evaporator for highly efficient water desalination. Energy Environ. Sci. **11**, 1985–1992 (2018). https://doi.org/10.1039/C8EE00567B
65. X. Wu, Y. Wang, P. Wu et al., Dual-zone photothermal evaporator for antisalt accumulation and highly efficient solar steam generation. Adv. Func. Mater. **31**, 2102618 (2021). https://doi.org/10.1002/adfm.202102618
66. D. Fan, Y. Lu, H. Zhang et al., Synergy of photocatalysis and photothermal effect in integrated 0D perovskite oxide/2D MXene heterostructures for simultaneous water purification and solar steam generation. Appl. Catal. B Environ. **295**, 120285 (2021). https://doi.org/10.1016/j.apcatb.2021.120285
67. Y. Wang, X. Wu, B. Shao et al., Boosting solar steam generation by structure enhanced energy management. Sci. Bull. **65**, 1380–1388 (2020). https://doi.org/10.1016/j.scib.2020.04.036
68. Y. Lu, D. Fan, H. Xu et al., Implementing hybrid energy harvesting in 3D spherical evaporator for solar steam generation and synergic water purification. Solar RRL. 4, 2000232 (2020). https://doi.org/10.1002/solr.202000232